Journal of Thermal Analysis and Calorimetry
https://doi.org/10.1007/s10973-026-15288-8

Comparative thermal analysis of heat transfer fluid injection orientation in phase change material based latent heat thermal energy storage systems

Sana Dardouri[1,2] · Bendida Medjahed[3] · Müslüm Arıcı[4] · Abdelhamid Mokhtari[3] · Fayçal Bouhenni[3] · Jalila Sghaier[1]

Received: 9 September 2025 / Accepted: 2 January 2026
© The Author(s) 2026

Abstract

This study aims to experimentally investigate the influence of heat exchanger orientation and heat transfer fluid (HTF) injection direction on the thermal performance of a latent heat thermal energy storage (LHTES) system using a phase change material (PCM). A comparative analysis is conducted between horizontal and vertical double-pipe heat exchanger configurations, considering both top and bottom injection of the HTF. The experimental methodology involves systematic variations of inlet temperature and volumetric flow rate while monitoring temperature evolution, charging and discharging durations, heat transfer coefficients, and Nusselt numbers. The results demonstrate that the direction of HTF injection plays a critical role in governing heat transfer behavior. Top injection promotes faster charging by enabling the PCM to reach higher average temperatures, whereas bottom injection enhances convective heat transfer, yielding the highest Nusselt numbers and heat transfer coefficients, albeit with longer charging and discharging times. In the horizontal configuration, increasing the flow rate from 60 to 120 L h^{-1} reduces the charging time from 70 to 60 min, corresponding to an improvement of 14.2%. Discharge tests performed at inlet temperatures of 70 °C and 80 °C reveal performance reductions of 8.9% for the horizontal configuration, 43.3% for bottom injection, and 42.6% for top injection at a constant flow rate. Overall, the horizontal configuration exhibits the fastest thermal response during both charging and discharging processes, while bottom injection achieves the highest thermal efficiency. These findings highlight the importance of heat exchanger orientation and flow direction optimization for improving the performance of LHTES systems.

Keywords Heat exchanger · Phase change material · Latent heat thermal energy storage · Charging process · Discharging process · Heat transfer fluid flow direction

Abbreviations

HTF	Heat transfer fluid
HX	Heat exchanger
LHTES	Latent heat thermal energy storage
PCM	Phase change material
Nu	Nusselt number
Re	Reynolds number
SHES	Sensible heat energy storage
TES	Thermal energy storage

Symbols

A	Surface area, (m^2)
F	Liquid fraction (%)
C_p	Specific heat, (J kg^{-1} K^{-1})
d	Diameter of the inner pipe, (m)
D	Diameter of the outer shell, (m)
f	Melt fraction
h	Average heat transfer coefficient (W m^{-2} K^{-1})
L_h	Latent heat (J kg^{-1})
$\dot{m}$	Mass flow rate, (kg s^{-1})
Q	Cumulative thermal energy, (J)
Qs	Stored energy (J)

✉ Müslüm Arıcı
muslumarici@gmail.com

[1] Laboratory of Thermal and Thermodynamics of Industrial Processes (LTTHPI), National Engineering School of Monastir, University of Monastir, 5019 Monastir, Tunisia

[2] Department of Physics, Faculty of Sciences of Gafsa, University of Gafsa, Campus Sidi Ahmed Zarouk, 2112 Gafsa, Tunisia

[3] Laboratory of Numerical and Experimental Modeling of Mechanical Phenomena, Faculty of Science and Technology, University of AbdelhamidIbnBadis, Mostaganem, Algeria

[4] Mechanical Engineering Department, Engineering Faculty, Kocaeli University, 41001 Kocaeli, Turkey

Published online: 06 February 2026

$\dot{Q}$	Heat transfer rate, (W)
T	Temperature, (^{o}C)
t	Time, (s)
$\dot{V}$	Volume flow rate, (L h^{-1})
ρ	Density, (kg m^{-3})
$\boldsymbol{\lambda}$	Thermal conductivity (W m^{-1} K^{-1})

Subscripts

c/d	Charging and discharging phases
f	Fluid
in	Inlet
l	Liquid
m	Melting
n	Number of PCM temperature sensor
out	Outlet
s	Solid
Avs	Average of the solid phase
Avl	Average of the liquid phase
i	Initial

Introduction

Latent heat thermal energy storage (LHTES) systems based on phase change materials (PCMs) have emerged as attractive solutions due to their ability to store large amounts of energy at nearly constant temperatures [1–4]. These systems not only enhance energy efficiency but also offer opportunities for industrial waste heat recovery and improved thermal management in buildings, power plants, and solar energy applications [5]. A key challenge in practical implementation is the low thermal conductivity of PCMs, which slows both charging (melting) and discharging (solidification), reducing system responsiveness and efficiency.

To address this limitation, numerous strategies have been explored. Heat transfer enhancement techniques, such as extended surfaces (fins), turbulators (helical coils or wavy tubes), and conductive additives (metal particles or expanded graphite), have been used to improve thermal performance [6–9]. Additionally, innovative geometries inspired by nature, such as bionic leaf-shaped or golf ball-like PCM capsules, have been investigated to improve heat distribution and storage consistency [7, 8]. These efforts highlight the importance of design optimization in making LHTES systems more efficient and practical.

Beyond materials and geometry, the behavior and arrangement of the heat transfer fluid (HTF) play a critical role. Variations in flow conditions, including inlet temperature, flow rate, and injection direction, can strongly influence PCM melting and solidification [10–14]. While several numerical studies have examined PCM performance in LHTES systems [15–18], the influence of heat exchanger (HX) orientation, i.e., vertical versus horizontal, remains underexplored. Experimental studies, such as those by Hasan [19, 20] and Seddegh et al. [21], indicate that horizontal configurations generally enhance phase change rates, particularly under partial-load conditions, due to stronger natural convection effects. The impact of HTF injection direction is also significant but less studied. In vertical shell-and-tube systems, both top and bottom injection modes have been tested, with mixed findings on which is more effective [23–29]. For instance, Moghaddam and Ganji [29] reported that bottom injection enhanced melting by 13%, while Guo et al. [30] and Nie et al. [31] highlighted that top injection favors convection-dominant phases, whereas bottom injection benefits conduction-dominated stages. Despite these insights, the combined effects of HX orientation and HTF injection direction, particularly in double-pipe configurations, have received limited attention.

To fill this gap, the present work experimentally investigates the influence of HX orientation, HTF injection direction, inlet temperature, and flow rate in both vertical and horizontal double-pipe LHTES systems. This study aims to provide a nuanced, quantitative understanding of system dynamics and operational parameters in the presence of PCM. The findings are relevant to a broad range of thermal-fluid applications where heat transfer results from the interaction of forced and natural convection with phase change. Similar mechanisms occur in magnetized and chemically reactive nanofluid flows, rotating disk systems, wedge-shaped geometries, and stretching surfaces, where flow direction and thermal boundary conditions critically affect heat transport.

This study offers several novel contributions. It delivers a real-world comparison of horizontal and vertical configurations while systematically evaluating top and bottom HTF injection strategies. While the work deliberately excludes active heat transfer enhancements such as fins and does not consider long-term effects like repeated thermal cycling or PCM aging, it still provides experimentally validated insights into key operational parameters, offering guidance for faster, more efficient, and responsive energy storage systems. Moreover, the observed trends can serve as benchmarks for future numerical simulations and intelligent optimization approaches, including neural-network-based thermal system design.

Experimental study

The experimental configuration for the water-PCM HX is depicted in Fig. 1. In this configuration, paraffin wax RT-50 is housed in the annular gap between an inner copper cylinder and an outer transparent acrylic envelope. The inner copper cylinder has dimensions of 16mm in outer diameter, a wall thickness of 1mm, and a length of 900mm. Hot water,

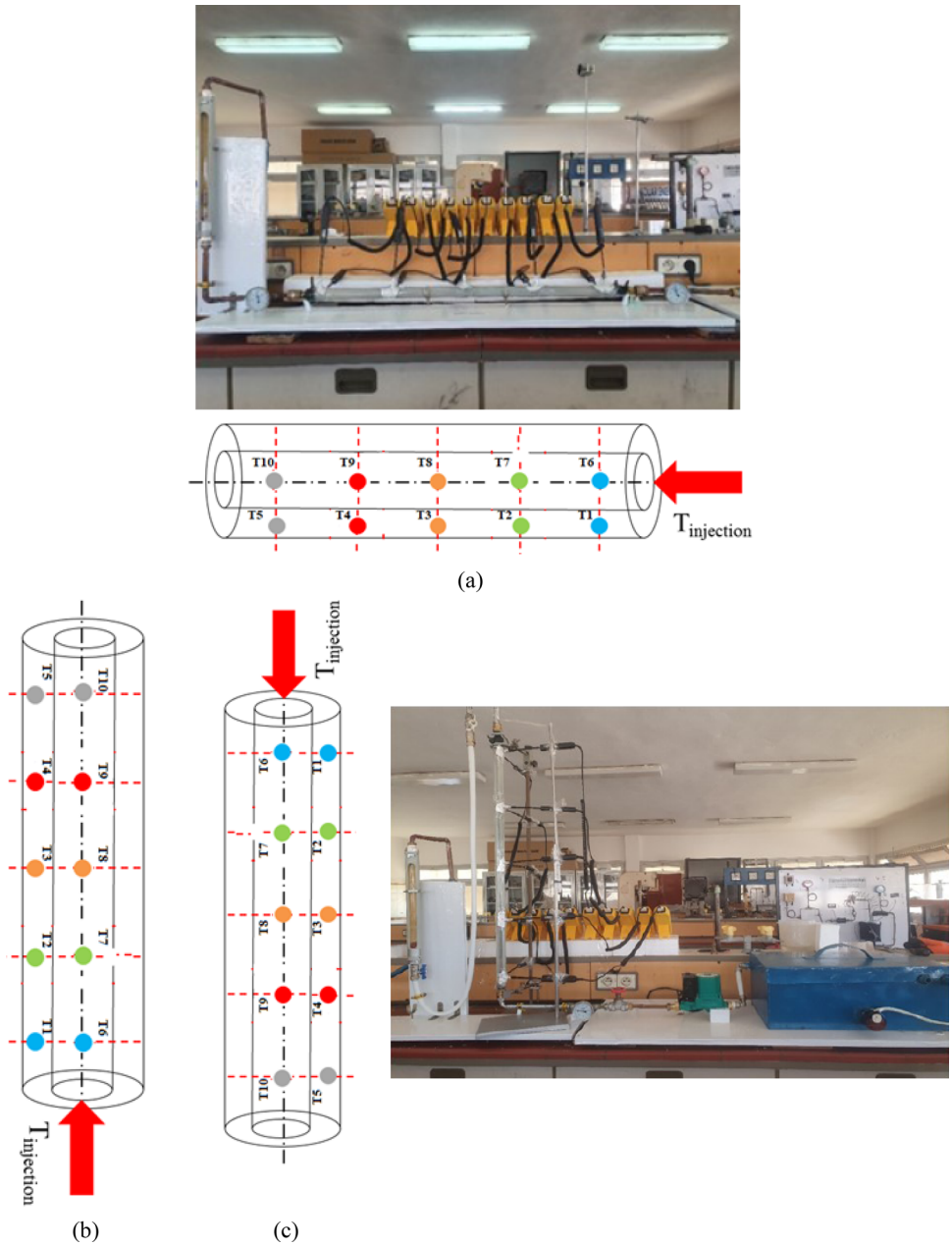


Fig. 1 Schematic diagram of the experimental setup; **a** horizontal right injection position, **b** vertical injection from the bottom position and **c** vertical injection from the top position

acting as the HTF, flows through the inner cylinder to convey thermal energy to the PCM. The outer acrylic envelope has an internal diameter of 24mm, a wall thickness of 2mm, and a length of 850mm. Its transparency permits observation of the PCM's melting process. Moreover, the acrylic shell features two outlets to facilitate the filling of liquid PCM and to manage volume changes during melting. The paraffin RT-50, used as the PCM, appears white in its solid state and turns transparent when melted. The thermophysical properties of paraffin RT-50 are detailed in Table 1.

In each experiment, water was heated in the tank and then introduced into the storage system via the inlet valve, ensuring the temperature was sufficiently high to compensate for any heat losses in the piping system. The experiment was concluded once the solid PCM had completely melted. Temperature values from all thermocouples were continuously monitored throughout the process. The HTF temperature was kept constant at 70 °C to evaluate its effect on the melting process. Three different HTF volume flow rates (60, 90, and 120 L h^{-1}) were tested in all experiments. To assess the reproducibility of the experiment, each experiment was conducted three times to ensure the reliability of the results.

Table 1 HX and PCM details

HX	Pipe material	Copper
PCM Paraffin RT-50 [36]	Container material	Plexiglas 10mm
	Container width × length × height	253mm × 310mm × 62mm
	PCM mass	200g
	Tube length	900mm
	Tube inner diameter (Copper)	12mm
	Tube outer diameter (Copper)	14mm
	Tube inner diameter (Plexiglas)	24mm
	Tube outer diameter (Plexiglas)	30mm
	Density ρ(kg•m^{-3})	760
	Specific heat C_p(kJ•kg^{-1}•K^{-1})	2
	Thermal conductivity λ(W•m^{-1}•K^{-1})	0.2
	Latent heat L_h(kJ•kg^{-1})	160
	Melting temperature T_f(°C)	45–51

Table 2 Precision of experimental devices

Devices	Parameters	Precision
Pt100 contact thermometer	− 50to + 199.9 °C	± 0.5 °C
Flowmeter	5 to 250L h^{-1}	± 5%

Uncertainty analysis

Table 2 presents a comprehensive overview of the uncertainties associated with the experimental devices. Based on the error propagation analysis [37], the highest uncertainties for the total heat stored or released and the mean temperature of the PCM, as calculated from Eqs. (1) and (2), are roughly 10.4% and ± 1.3%, respectively.

$$\delta\overline{Q}_{c/d} = \int_0^t \left[\left(\frac{\partial \overline{Q}_{c/d}}{\partial \dot{V}} \delta \dot{V} \right)^2 + \left(\frac{\partial \overline{Q}_{c/d}}{\partial T_{in}} \delta T_{in} \right)^2 + \left(\frac{\partial \overline{Q}_{c/d}}{\partial T_{out}} \delta T_{out} \right)^2 \right]^{1/2} dt \tag{1}$$

$$\delta\overline{T}_{PCM} = \frac{1}{5}\left[\left(\frac{\partial \overline{T}_{PCM}}{\partial T_1} \delta T_1 \right)^2 + \left(\frac{\partial \overline{T}_{PCM}}{\partial T_2} \delta T_2 \right)^2 + \ldots + \left(\frac{\partial \overline{T}_{PCM}}{\partial T_5} \delta T_5 \right)^2 \right]^{1/2} \tag{2}$$

Data analysis

During the experiments, temperatures were recorded for the inner pipe's surface and for the PCM at various points. The heat transfer rate ($\dot{Q}$) between the HTF (water) and the PCM was determined by:

$$\dot{Q} = \dot{m} c_p \left(T_{HW,in} - T_{HW,out} \right) \tag{3}$$

Here, $\dot{m}$ is the HTF's mass flowrate (kg s^{-1}); Cp denotes the specific heat capacity (J kg^{-1} K^{-1}); $T_{HW,in}$ indicates the inlet temperature of the hot water (K) and $T_{HW,out}$ represents the outlet temperature of the hot water (K).

A theoretical approach to evaluate the natural convection heat transfer coefficient in PCM involves obtaining the local heat transfer coefficient through specific calculations

$$h_{PCM} = \frac{\dot{Q}}{A_{PCM}\left(T_{HX} - T_{PCM} \right)} \tag{4}$$

where h_{PCM} is PCM side heat transfer coefficient (W m^{-2} K^{-1}); A_{PCM} is the total surface area to the PCM (m^2), T_{HX} and T_{PCM} are the temperature of HX and the liquid PCM (K), respectively. T_{HX} is taken the HTF's average temperature:

$$T_{HX} = \frac{\left(T_{HW,in} + T_{HW,out} \right)}{2} \tag{5}$$

The temperatures of the fluid at the inlet and outlet are represented by $T_{HW.in}$ and $T_{HW.out}$, respectively. The heat transferred from the inner surface of the tube to the PCM

was calculated using the average Nusselt number, which is defined as follows:

$$Nu_{\mathrm{PCM}} = \frac{h_{\mathrm{PCM}} L_{\mathrm{c}}}{\lambda_{\mathrm{PCM}}} \tag{6}$$

where h_{PCM} is the convective heat transfer coefficient of the PCM (W m^{-2} K^{-1}), L_c is the characteristic length (m), defined as $L_c = D - d$, where D and d represent the outer and inner diameters of the tube, respectively, and λ_{PCM} is the thermal conductivity of the PCM (W m^{-1} K^{-1}).

The thermal energy contained in the PCM comprises the sensible heat gained by both the solid and liquid phases, along with the latent heat stored throughout the phase transition. The amount of stored energy can be calculated as [38]:

$$H_n = m_{\mathrm{PCM}}\left[C_{p,s}\left(T_{avs} - T_i\right)(1-f) + f\,L_h + f\,C_{p,l}\left(T_{avl} - T_l\right)\right] \tag{7}$$

In this context, T_{avs},T_{avl}, and $T_i$refer to the average temperatures of the solid phase, the liquid phase, and the initial temperature, respectively. Furthermore, f signifies the liquid fraction.

Results and discussion

In this section, we present the results and discussions from our experimental investigation into the impact of heat exchanger configurations on the performance of PCM charging and discharging. Specifically, we explored how horizontal and vertical heat exchanger orientations, as well as the mode of HTF injection (bottom vs. top), influence the efficiency and optimization of these processes.

Charging process

During the charging process, heat transfer occurs due to the temperature difference between the HTF and the PCM. Initially, when the PCM is solid, heat is conducted through its structure until it reaches the melting point. At this stage, latent heat absorption drives the phase transition, gradually liquefying the PCM. Once fully melted, heat transfer continues mainly through convection within the liquid PCM. The experiment ensured a full phase change by maintaining the HTF temperature well above the PCM's melting point, with the process concluding once thermal equilibrium was reached. In this work, the starting temperature of the PCM was adjusted to approximately 21 °C, which corresponds to ambient temperature. Charging process commenced when the temperature variation among all thermocouples was under 1 °C and terminated when $T_{HW.in}$- $T_{HW.out} \leq 6$ °C was reached. Melting process was conducted at different HTF flow rates, and the outcomes were subsequently examined.

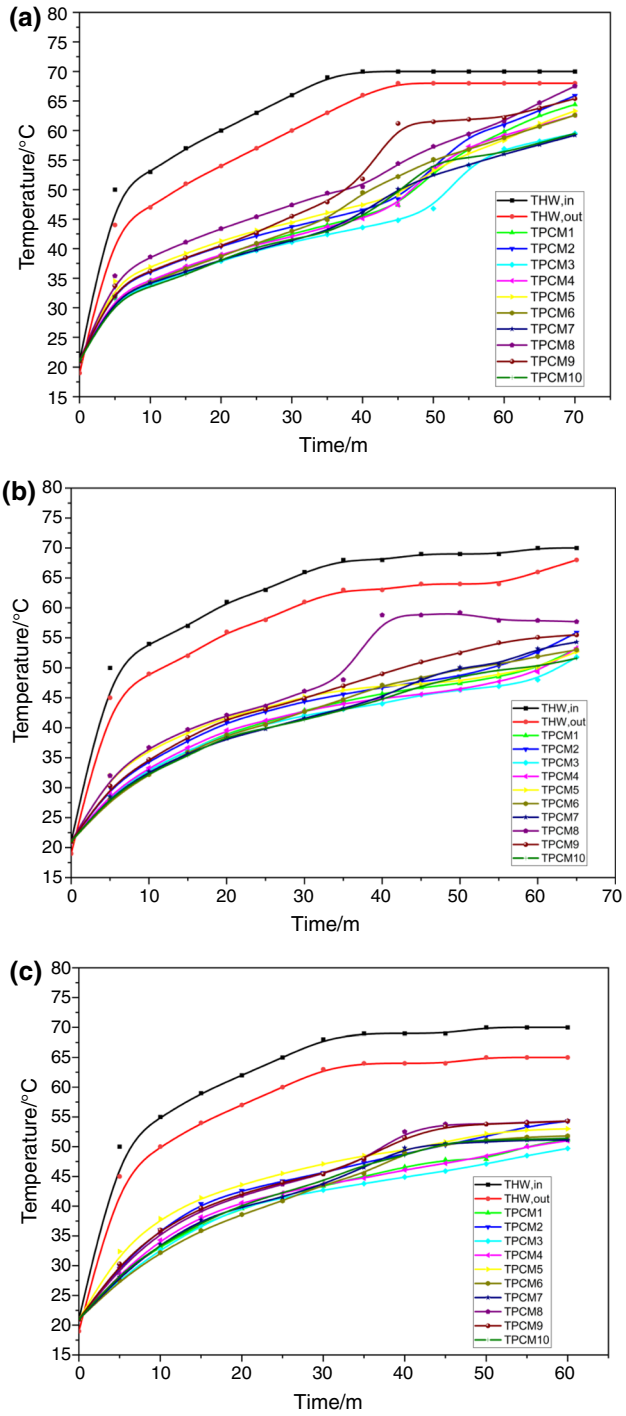


Fig. 2 Temperature profiles during the melting process for various HTF flowrates **a**) 60L h^{-1}, **b**) 90L h^{-1}, and **c**) 120L h^{-1} of the axial position during a horizontal load

Figure 2 presents the temperature measurements during the charging phase for the horizontal configuration at flow rates of 60, 90, and 120 L h^{-1}. Analysis of the HTF flow rate's impact on melting temperature profiles reveals a clear trend: as the flow rate increases, PCM temperatures decrease.

At 60 L h^{-1}, PCM temperatures range from 59.5 to 65.9 °C at 0° and from 59.2 to 67.5 °C at 90°. Increasing the flow rate to 90 L h^{-1} lowers these values to 51.8–55.9 °C at 0° and 51.6–57.7 °C at 90°. At 120 L h^{-1}, temperatures drop further, ranging from 49.7 to 54.3 °C at 0° and 51.1 to 54.3 °C at 90°.

This trend indicates that higher flow rates enhance heat transfer efficiency, leading to lower PCM temperatures and a narrower temperature range, signifying improved thermal homogenization. Higher flow rates facilitate more effective heat removal, resulting in a more uniform temperature distribution and enabling precise control of the melting process.

At a low flow rate (60 L h^{-1}), temperature variations are more pronounced. A moderate flow rate (90 L h^{-1}) improves uniformity, while a high flow rate (120 L h^{-1}) achieves the best temperature homogenization. Additionally, charging time decreases with increasing flow rate: 70 min at 60 L h^{-1}, 65 min at 90 L h^{-1}, and 60 min at 120 L h^{-1}. This reduction confirms that higher flow rates accelerate thermal transfer, leading to faster and more efficient charging, as demonstrated by Martinelli et al. [39] and Hassan et al. [40].

Figure 3 illustrates the variation in PCM temperature over time during the melting phase, with a constant HTF flow rate of 60 L h^{-1} and initial HTF temperatures of (a) 70 °C and (b) 80 °C. To evaluate the feasibility of this setup for industrial applications, horizontal charging tests were conducted, considering the impact of gravity when the system was oriented to the right. Water can be introduced from the right through a valve system, and images captured during this process are presented in Fig. 3a.

In this configuration, the melting front primarily progresses through the center of the test section, while solid PCM remains at both the top and bottom of the heat exchanger. This is due to the presence of peripheral tubes and headers, as well as liquid motion that pushes the PCM upward. Analyzing temperature profiles based on angular position provides deeper insight into the key heat transfer mechanisms in this setup.

During the initial melting phase, lasting approximately 1,200 s, heat transfer is primarily influenced by the water temperatures of 70 °C and 80 °C. At 80 °C, natural convection begins to develop within 20 min, accelerating the melting process in the upper half of the cell. As these convection currents intensify, they further enhance melting in the upper region across different water temperatures. However, as the process advances, the overall melting rate declines. This reduction occurs because thermal energy from the HTF concentrates in the upper section, leaving the lower region with insufficient heat to fully melt the solid PCM. Consequently, overheating and thermal stratification occur at the top of the storage unit. Higher HTF temperatures positively impact the melting rate, as demonstrated in Fig. 3b. When the HTF temperature increases from 70 to 80 °C, the melting time decreases by approximately 25%, reducing from around 3,600 s at 70 °C to 2,700 s at 80 °C, as observed by Martinelli et al. [39].

Figures 4–6 depict the temperature profiles during the melting process, including the inlet temperature, outlet temperature, and the average PCM temperature. These profiles are analyzed for HTF flow rates of (a) 60 L h^{-1}, (b) 90 L h^{-1}, and (c) 120 L h^{-1}, at different axial positions for horizontal, bottom and top loading configurations. Data analysis reveals that the heat exchanger's orientation significantly impacts the PCM melting efficiency. When the HTF inlet is positioned at horizontal, the system achieves higher average PCM temperatures and shorter charging times compared to the top and the bottom inlet configuration, respectively. For instance, at an HTF flow rate of 60 L h^{-1}, the PCM's average temperature in the horizontal injection setup reaches 62.99 °C, whereas in the top/bottom configuration, it remains at 55.89 °C/48.96 °C, despite the shorter charging time in the horizontal configuration and the longer charging time in the top configuration. This indicates that top injection enhances heat transfer efficiency. Additionally, increasing the HTF flow rate whether 60, 90, or 120 L h^{-1} raises the PCM's average temperature and reduces charging times in both configurations. However, the benefits are more pronounced with top injection. At 120 L h^{-1}, the PCM's average temperature reaches 58.92 °C with a charging time of 90 min, whereas in the bottom configuration, it only reaches 50 °C with a charging time of 80 min. To optimize melting efficiency, employing the top injection configuration alongside a high HTF flow rate is recommended, as this combination maximizes heat transfer and minimizes melting time. Similar findings have been reported by [41, 42].

Figure 7 presents images of the melting process for both bottom and top charging, illustrating the evolution of the melting fronts over time. In Fig. 7a (top charging), the PCM surrounding the central tube begins melting first, progressing from top to bottom in alignment with the coolant fluid's injection direction. The hot liquid PCM rises due to volumetric expansion and natural convection, creating a chimney effect. This circulation promotes the gradual melting of the remaining solid PCM along the edges of the test section. At 3000 s, the melting front reaches the midpoint of the exchanger, and complete melting occurs by 4800 s. Conversely, Fig. 7b (bottom charging) shows a relatively horizontal melting front. The observed melting fronts at the periphery of the test section do not fully reveal the internal melting dynamics. Previous research suggests that the internal front is axisymmetric and inclined relative to the tube. Circulation between the liquid and solid phases continues to erode the solid PCM, but at a slower rate. At 3000 s, the melting front reaches the midpoint, but complete melting takes 6000 s. Overall, the results indicate that bottom

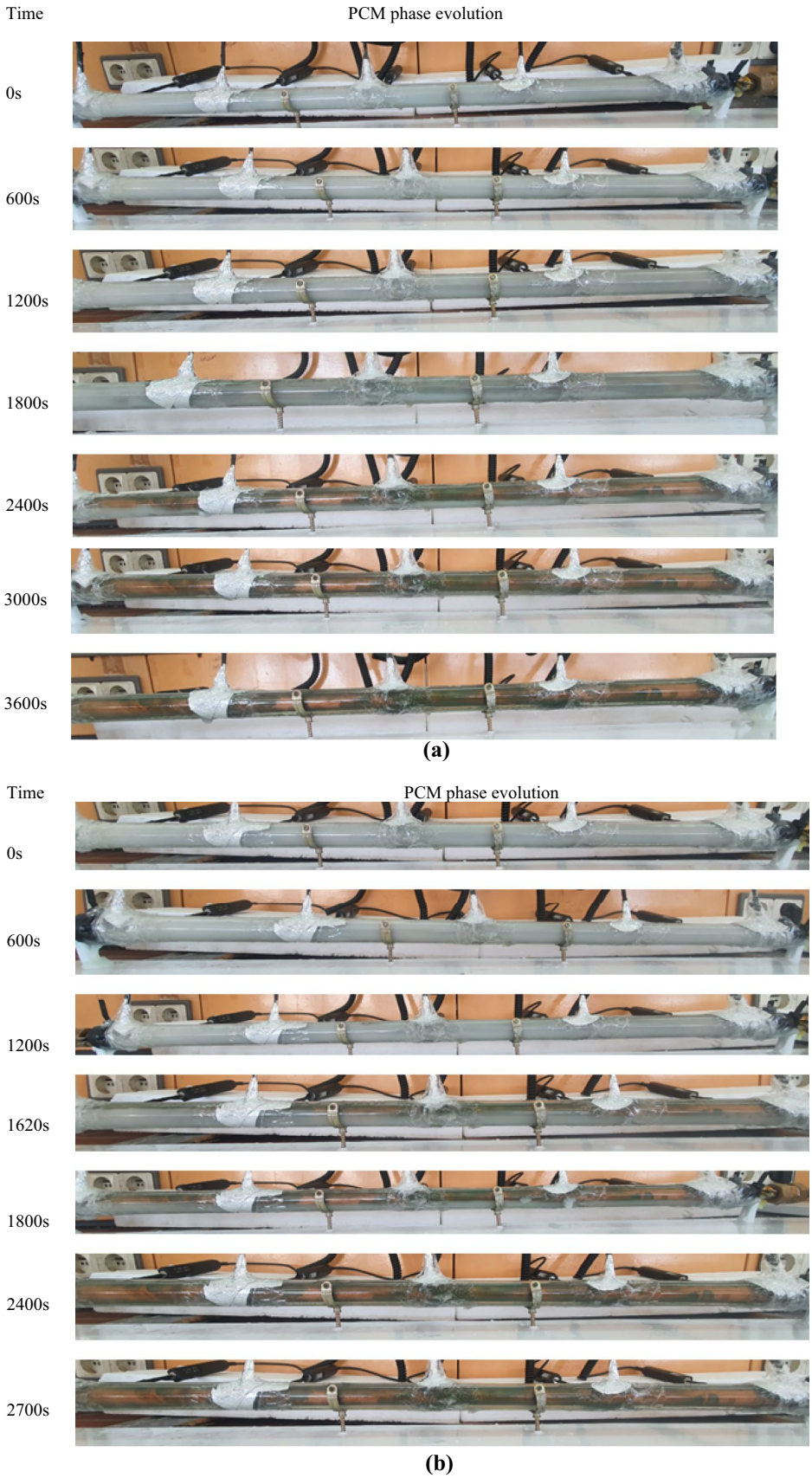


Fig. 3 Temporal evolution of the PCM temperature throughout the melting process at a steady HTF flow rate of60 L h^{-1} and an initial HTF temperature of **a** 70°C and **b** 80°C

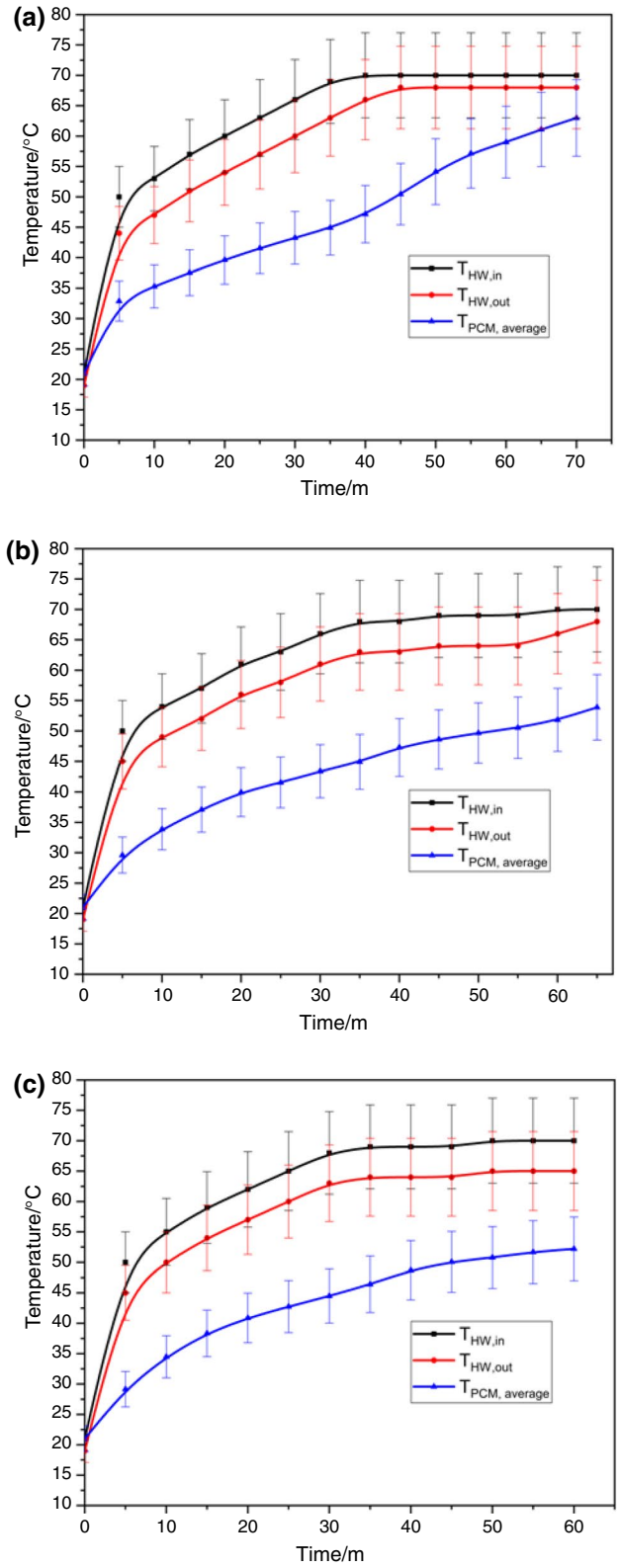


Fig. 4 Temperature profiles during melting process ($Th_{HW,in}$, $T_{HW,out}$, and $T_{PCM,moy}$) for various HTF flowrates **a**) 60L h, **b**) 90L h^{-1}, and **c**) 120L h^{-1} of the axial position during a horizontal

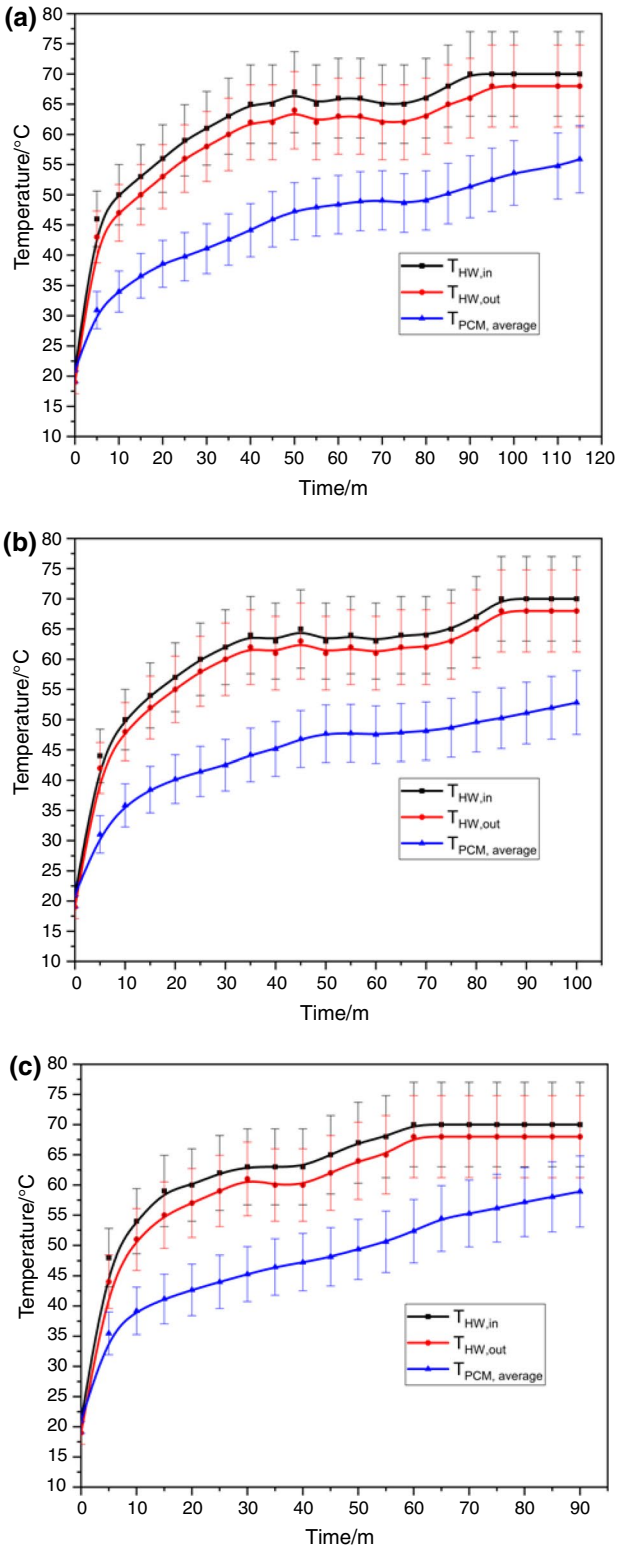


Fig. 5 Temperature profiles during melting process ($Th_{HW,in}$, $T_{HW,out}$ and $T_{PCM,moy}$) for various HTF flowrates **a**) 60L h^{-1}, **b**) 90L h^{-1}, and **c**) 120L h^{-1} of the axial position during a load from the bottom

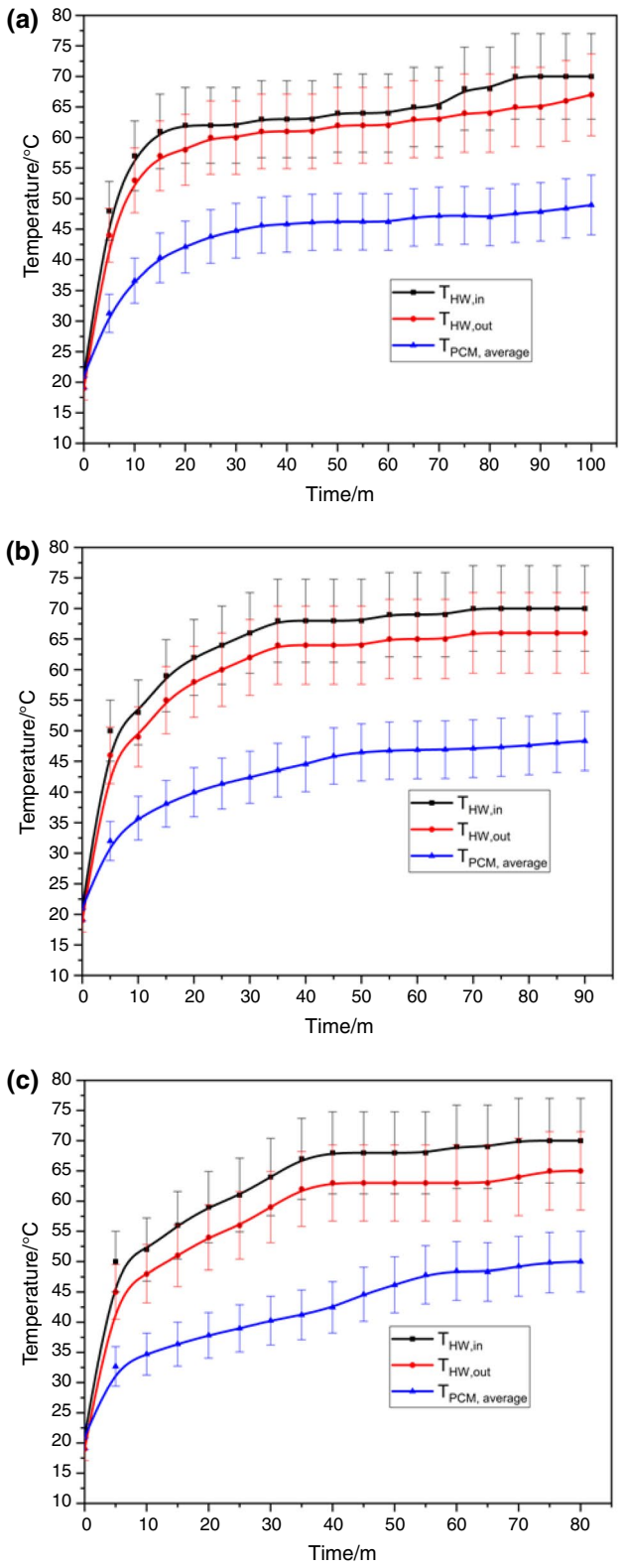


Fig. 6 Temperature profiles during melting process ($Th_{HW,in}$, $T_{HW,out}$ and $T_{PCM,moy}$) for various HTF flowrates **a**) 60L h^{-1}, **b**) 90L h^{-1}, and **c**) 120L h^{-1} of the axial position during a load from the top at 70 °C

charging requires 6000 s, whereas top charging completes in 4800 s, confirming that bottom injection is the slower process.

Discharging process

Physically, the heat transfer during discharging occurs due to the temperature difference between the PCM and the HTF. Initially, when the PCM is in its liquid state, heat is transferred primarily through convection within the PCM and conduction at the interface with the HTF. As the temperature decreases to the phase transition point, latent heat release governs the process, causing the PCM to solidify gradually. Once solidification is complete, further cooling occurs solely through conduction within the solid PCM. Discharging experiments were conducted with the HTF inlet at ambient temperature, while the initial PCM temperature was approximately 70 °C, well above its melting point to ensure a complete observation of the process. The process concluded when both the PCM and water temperatures dropped below 28 °C, typically ranging between 24 and 27 °C. During these tests, the PCM temperature evolution, as well as the HTF inlet and outlet temperatures, were monitored at flow rates of 60, 90, and 120 L h^{-1}. Results for the bottom, top, and horizontal configurations are presented in Figs. 8–10, with temperature curves illustrating the HTF behavior at both the inlet and outlet of the test section. The initial injection temperature for discharging was approximately 20 °C, though minor variations occurred at the start due to thermal inertia. Prior to testing, the test section was stabilized at the charging temperature using a stabilization circuit, while the measurement circuit operated at a lower temperature. Analysis of the temperature profiles during solidification reveals that HTF flow rate and system configuration significantly influence thermal efficiency. In all three configurations (horizontal, bottom, and top), higher flow rates enhance thermal discharge efficiency by reducing the time required for heat extraction. For example, in the horizontal configuration, increasing the flow rate to 120 L h^{-1} shortens the discharge time to 38 min, compared to 54 min at 60 L h^{-1}. Similarly, in the bottom and top configurations, discharge times decrease from 60 to 46 min and 56 to 44 min, respectively, as flow rates increase. Although the HTF outlet temperature remains stable between 25 and 27 °C, the average PCM temperature decreases more gradually at higher flow rates. For instance, in the bottom configuration at 120 L h^{-1}, the PCM temperature drops from 58.53 to 24.11 °C, whereas at 60 L h^{-1}, it declines from 55.89 to 22.85 °C. These results indicate that higher flow rates improve thermal extraction efficiency, reducing discharge time while maintaining a relatively stable final PCM temperature, primarily influenced by system configuration. In summary, increasing the HTF flow rate enhances heat transfer efficiency and shortens discharge

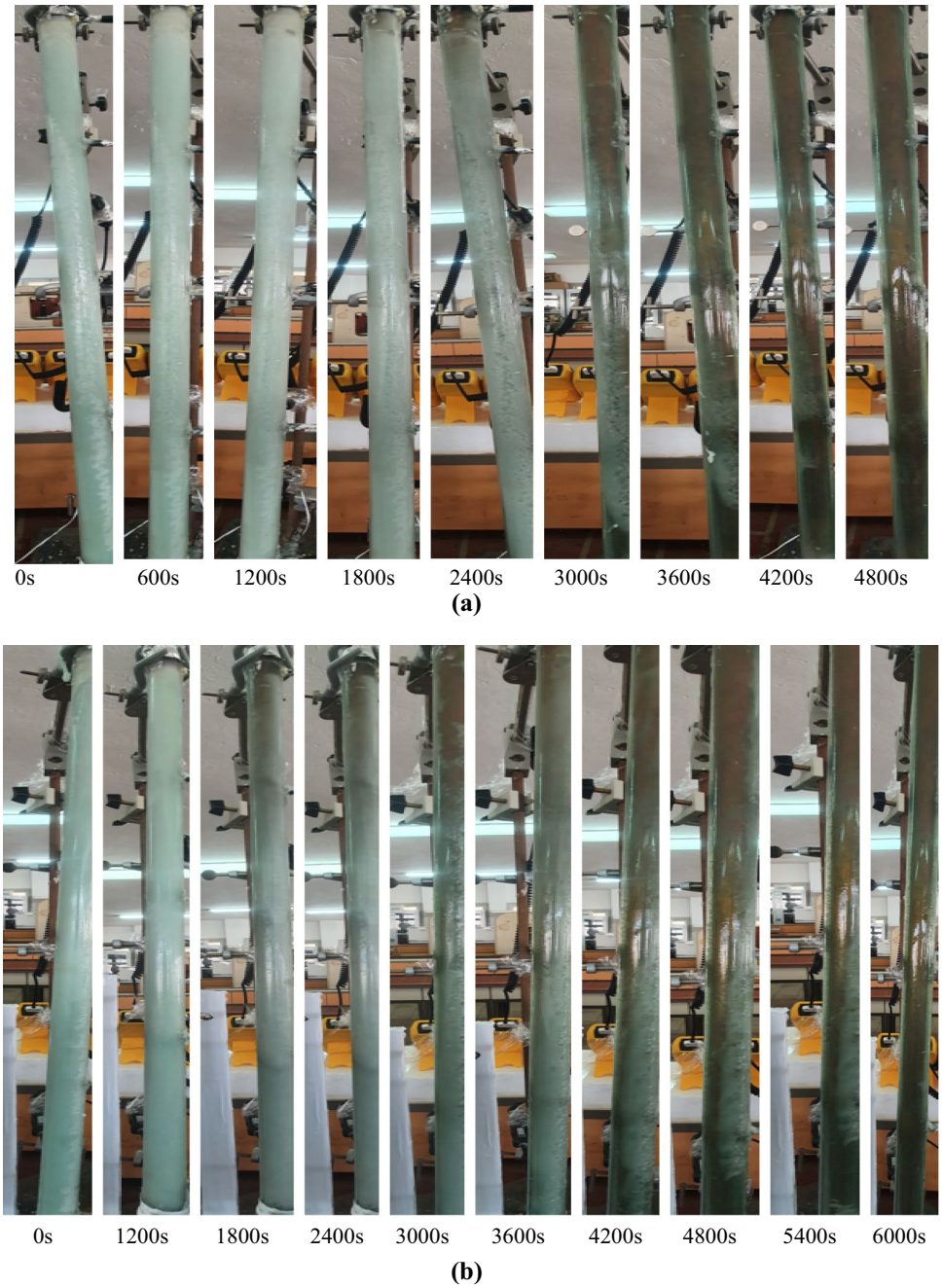


Fig. 7 Temporal evolution of the PCM temperature throughout melting process at a steady HTF flowrate of 60 L h^{-1} and an initial HTF temperature at 70 °C for **a**) Injection from top and **b**) Injection from bottom

time, while PCM temperature variations are primarily dependent on the configuration used, as demonstrated by Kalapala et al. [42].

Figure 11 presents real-time images of RT50 solidification at $\dot{m} = 60$ L h^{-1}, comparing two water temperatures (70 °C and 80 °C) across three HTF injection positions: horizontal, bottom, and top. Each injection method exhibits distinct characteristics that influence solidification and heat transfer.

- Horizontal injection enables even material distribution, potentially reducing testing time for tubular geometries. However, it may create localized overpressures due to complex solidification fronts, complicating the management of partial discharges and storage.
- Bottom injection promotes thermal stratification, leading to faster solidification as the thermocouple is positioned lower in the exchanger. While this method effectively controls heat flow, it may result in less uniform temperature distribution and thermal gradients.

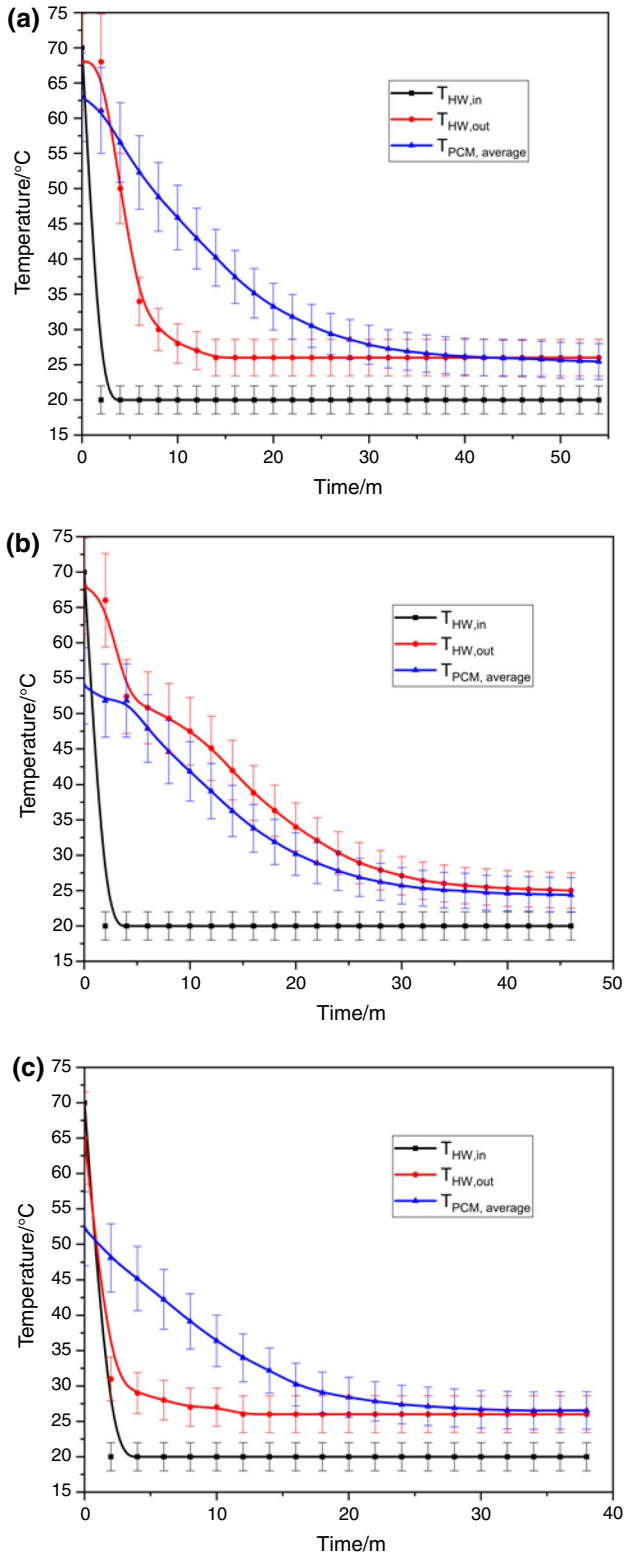


Fig. 8 Temperature profiles during solidification process for HTF flowrates **a**) 60L h^{-1}, **b**) 90L h^{-1}, and **c**) 120L h^{-1} of the axial position during a horizontal discharge

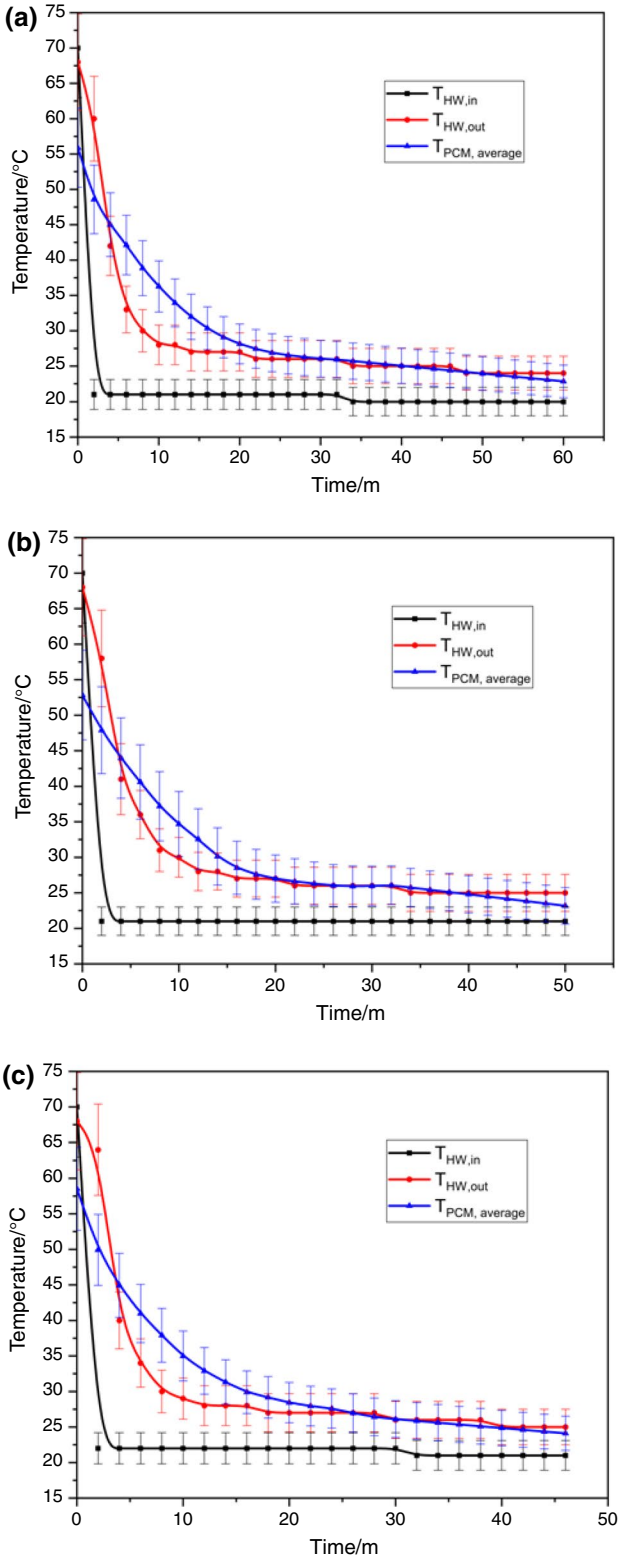


Fig. 9 Temperature profiles during solidification process for HTF flow rates **a**) 60L h^{-1}, **b**) 90L h^{-1}, and **c**) 120L h^{-1} of the axial position during a discharge from the bottom at 70 °C

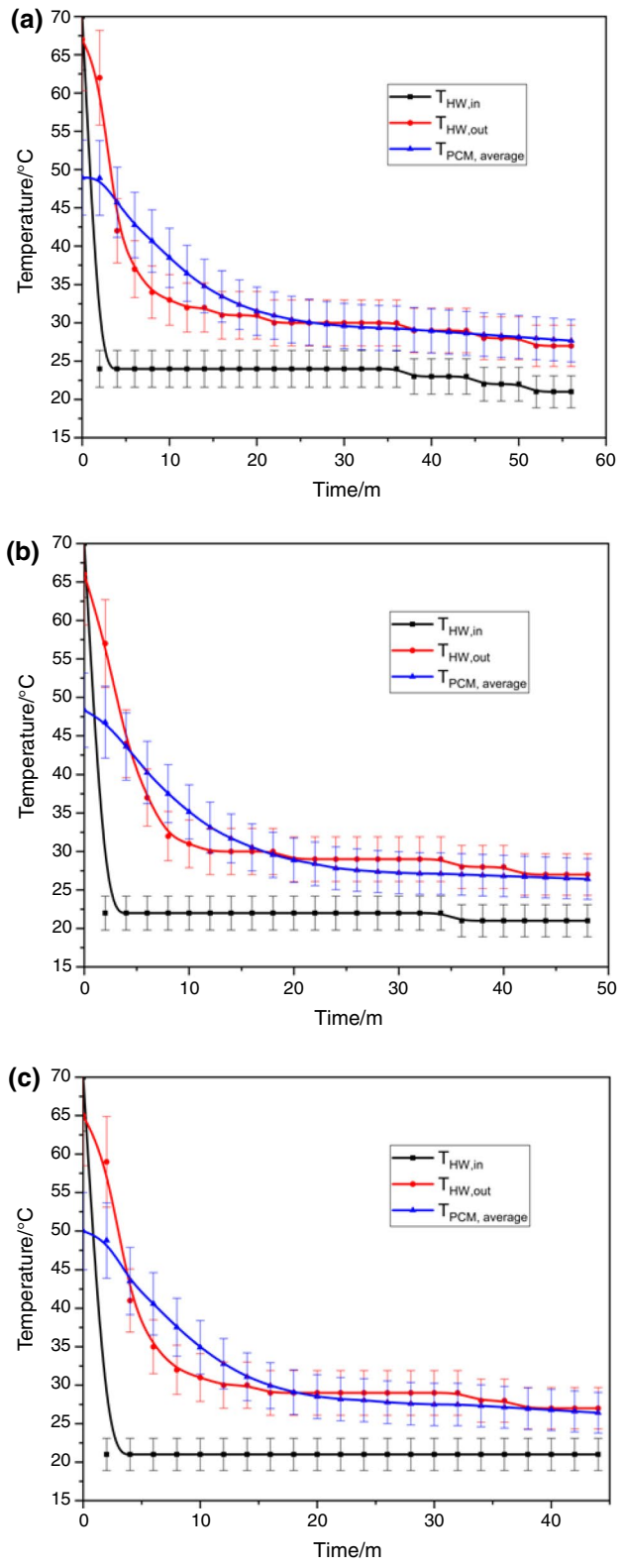


Fig. 10 Temperature profiles during solidification process for HTF flow rates **a**) 60L h^{-1}, **b**) 90L h^{-1}, and **c**) 120L h^{-1} of the axial position during a discharge from the top at 70 °C

- Top injection, which is particularly beneficial for industrial applications, allows for efficient management of partial charging and discharging. It ensures controlled temperature distribution along the axis, which is crucial for optimizing performance during discharge phases.

Thus, the choice of injection configuration should be based on specific application needs, weighing the advantages and limitations of each approach. Analyzing the results at 70 °C and 80 °C with a steady flow of 60 L h^{-1} reveals significant differences in discharge times:

- Horizontal discharges last over 56 min at 70 °C and decrease to 51 min at 80 °C, a reduction of approximately 8.9%.
- Bottom discharges drop from over 60 min to 34 min, indicating a 43.3% reduction.
- Top discharges reduce from over 54 min at 70 °C to over 31 min at 80 °C, reflecting a 42.6% decrease.

These results highlight that higher water temperatures significantly reduce discharge times, enhancing overall process efficiency.

Comparative study

To compare the experimental results with theoretical calculations of the heat transfer coefficient (h), Fig. 12 illustrates the variation in its average value. This coefficient plays a crucial role in determining the efficiency of heat exchange between the HTF and PCM. A higher h enhances heat transfer, thus accelerating both the charging and discharging processes. Due to the significant variation in experimental values of h, which depends on both the PCM temperature and the measurement location, it is essential to determine average values within specific intervals. In this study, three temperature ranges were considered 45–51 °C, corresponding to the theoretical phase transition of the PCM; 51–55 °C, representing the liquid phase; and temperatures above 55°C. Additionally, Fig. 12 shows the average temperature of the heat exchanger (T_{HX}) during the PCM charging process, along with the average temperature of the PCM in its liquid phase (T_{PCM}), obtained from all temperature sensor readings. To enable a detailed analysis and comparison with experimental data, the evaluation focuses on three temperature intervals: 45–51 °C, 51–55 °C, and above 55 °C.

The results indicate that the average h increases with higher flow rates. In the 45–51 °C range, the bottom water injection configuration achieves an average h of 592.849 W m^{-2} K^{-1} at a flow rate of 60 L h^{-1}, rising to 904.9 W m^{-2} K^{-1} at 90 L h^{-1} and further increasing to 1176.38 W m^{-2}

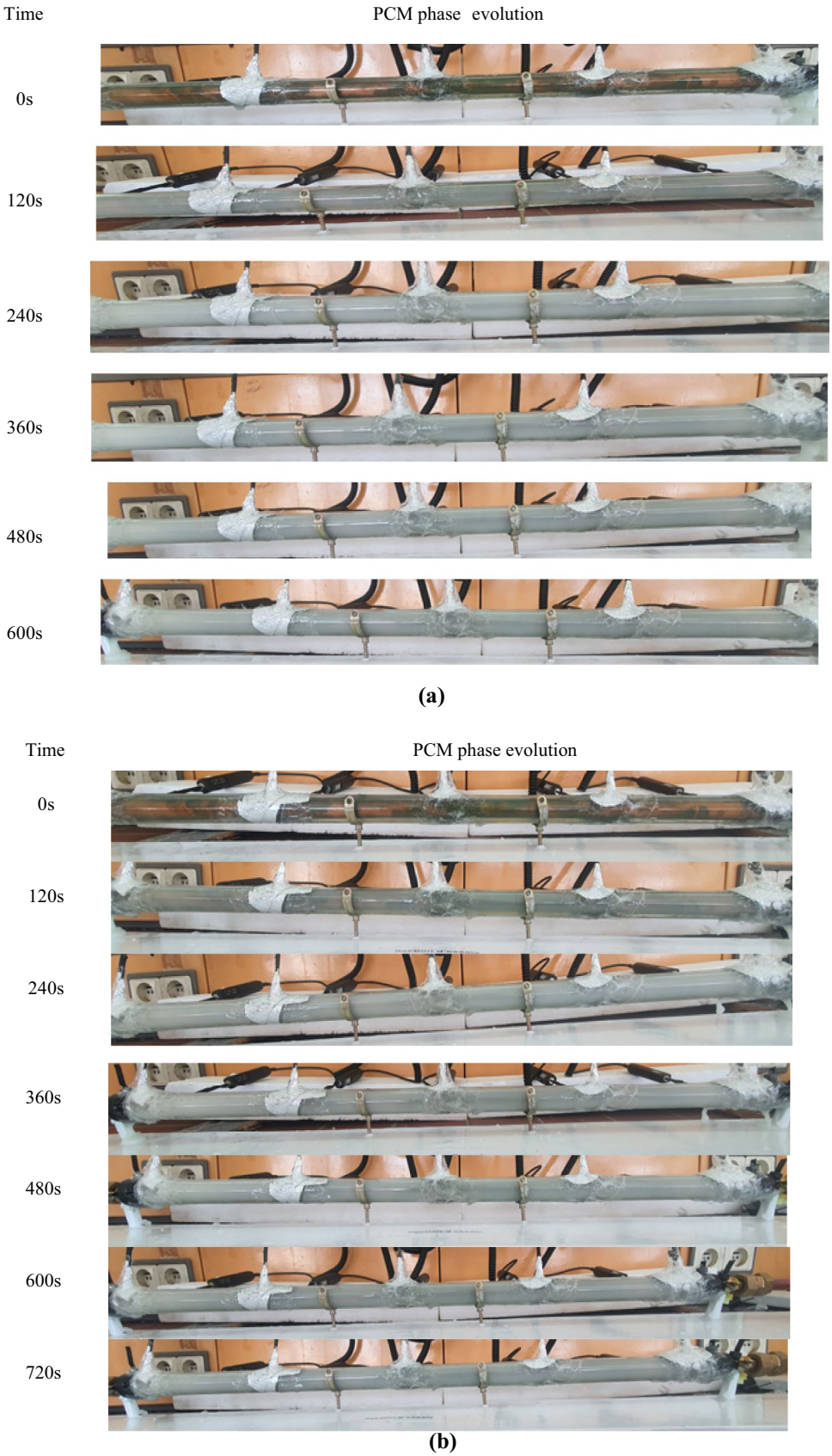


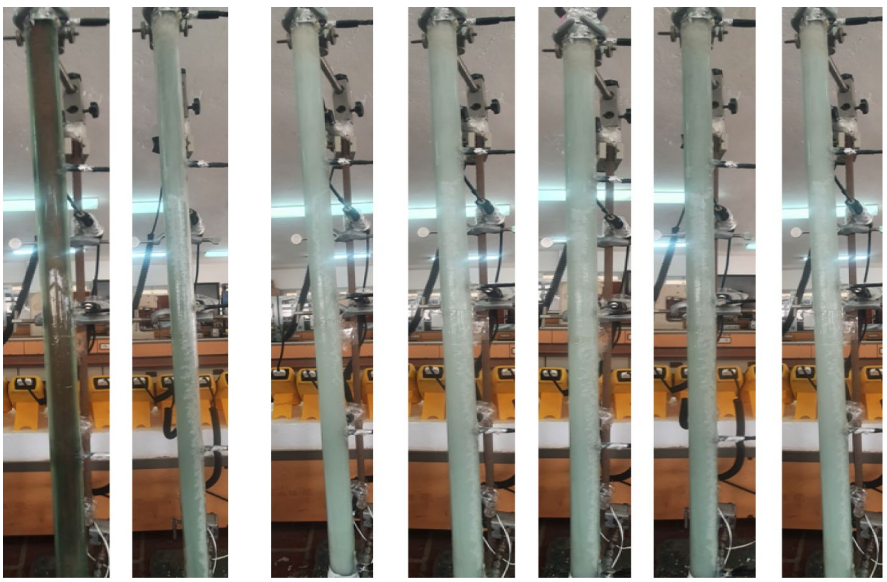
Fig. 11 Real-time images capturing the solidification of RT50 at flow rate of 60L h^{-1} and across different water temperatures for **a**) horizontal HX at T = 70°C, **b**) horizontal HX at T = 80°C, **c**) vertical HX with HFT injection from bottom at T = 70°C, **d**) vertical HX with HFT injection from bottom at T = 80°C, **e**) vertical HX with HFT injection from top at T = 70°C, and **f**) vertical HX with HFT injection from top at T = 80°C

Fig. 11 (continued)



0s 120s 240s 360s 480s 600s 720s 840s 960s

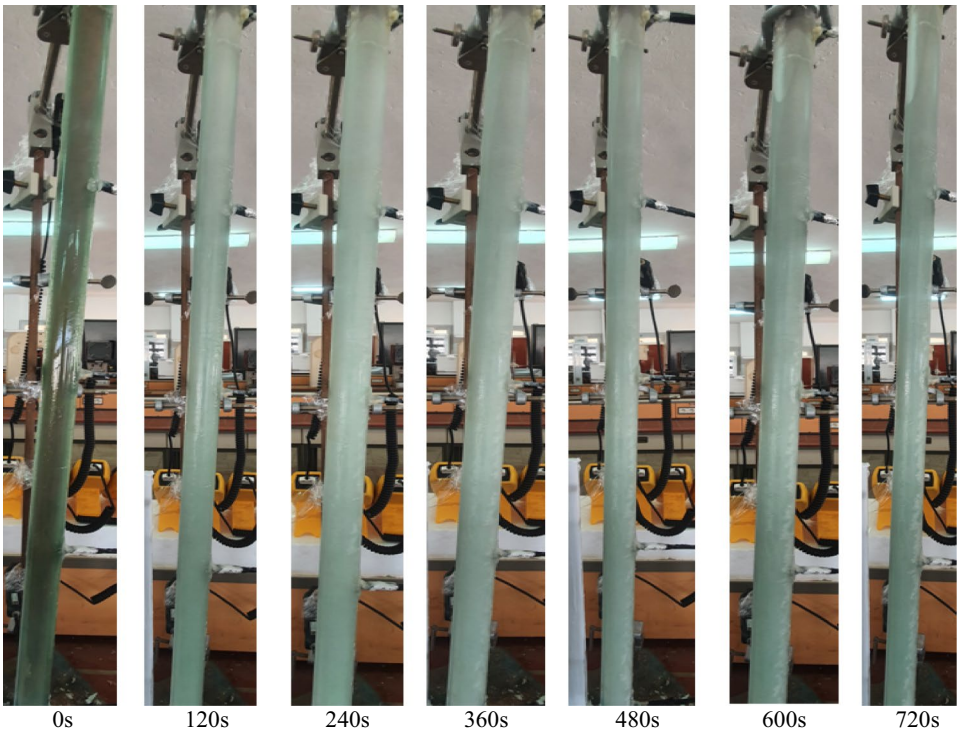
(c)



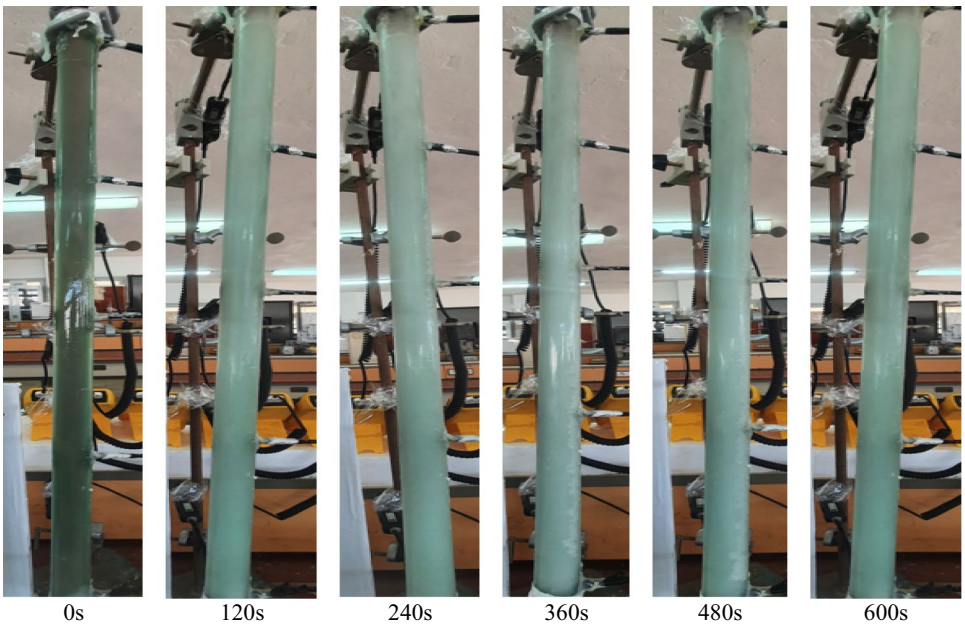
0s 120s 240s 360s 480s 600s 720s

(d)

Fig. 11 (continued)



(e)



(f)

K^{-1} at 120 L h^{-1}. For the top water injection configuration, h starts at 530.85 W m^{-2} K^{-1} at 60 L h^{-1}, increases to 744.271 W m^{-2} K^{-1} at 90 L h^{-1}, and reaches 1097.874 W m^{-2} K^{-1} at 120 L h^{-1}. The horizontal water injection setup shows a similar trend, with h values of 398.664 W m^{-2} K^{-1} at 60 L h^{-1}, 557.709 W m^{-2} K^{-1} at 90 L h^{-1}, and 962.968 W m^{-2} K^{-1} at 120 L h^{-1}. These findings demonstrate a positive correlation between flow rate and heat transfer efficiency across all configurations.

For the 51–55 °C range, the bottom injection configuration records an h of 622.96 W m^{-2} K^{-1} at 60 L h^{-1}, increasing to 882.62 W m^{-2} K^{-1} at 90 L h^{-1} and 1653.14 W m^{-2}

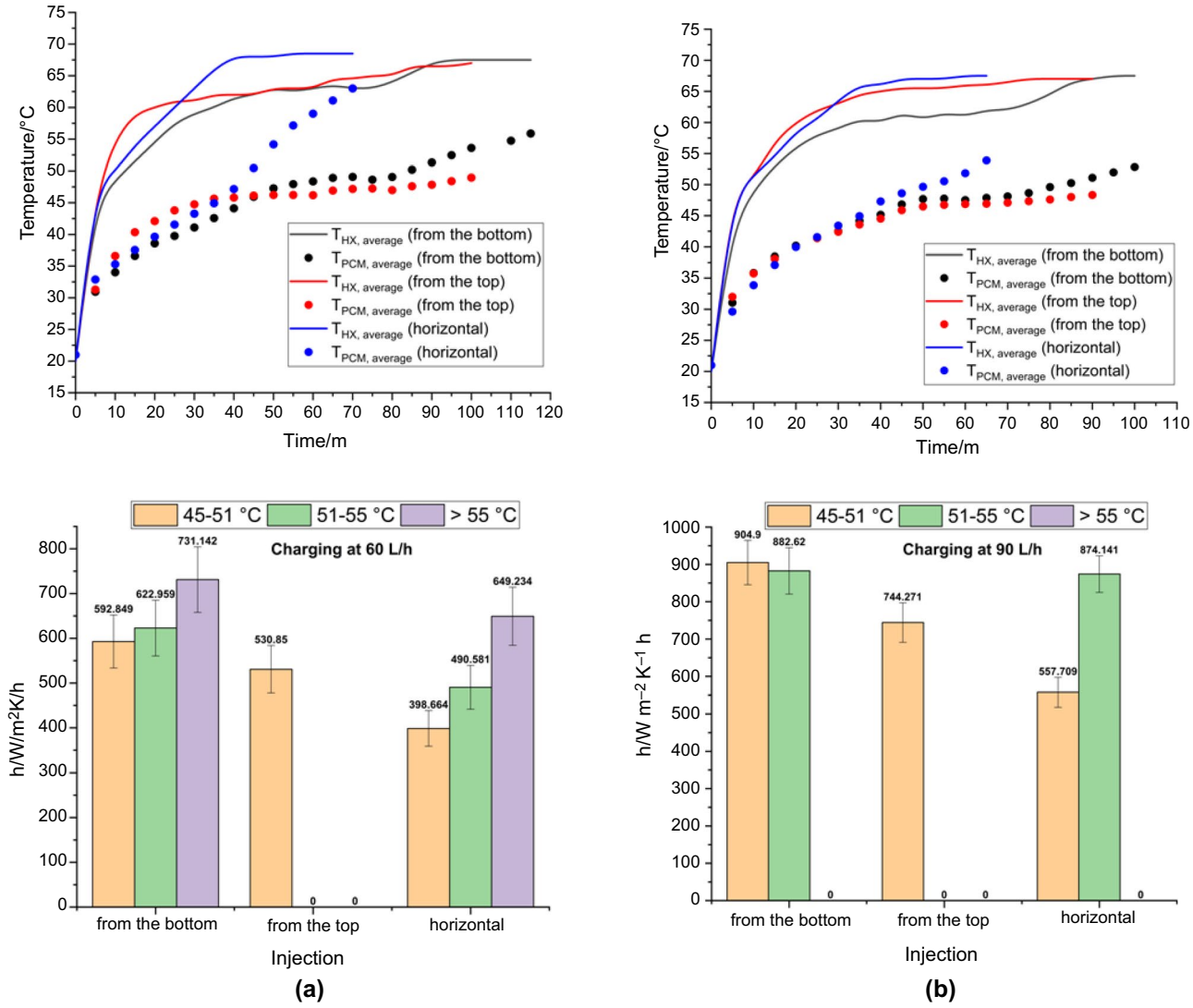


Fig. 12 Temperature distribution and average heat transfer coefficient for horizontal configuration at flowrate of **a**) 60L h^{-1}, **b**) 90L h^{-1}, and **c**) 120L h^{-1}

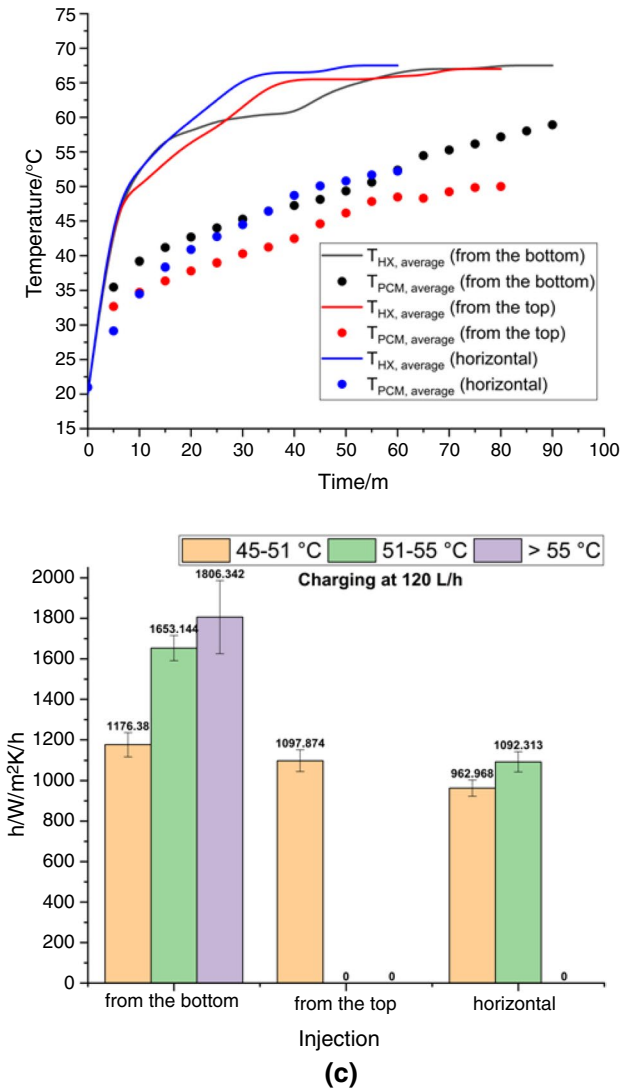


Fig. 12 (continued)

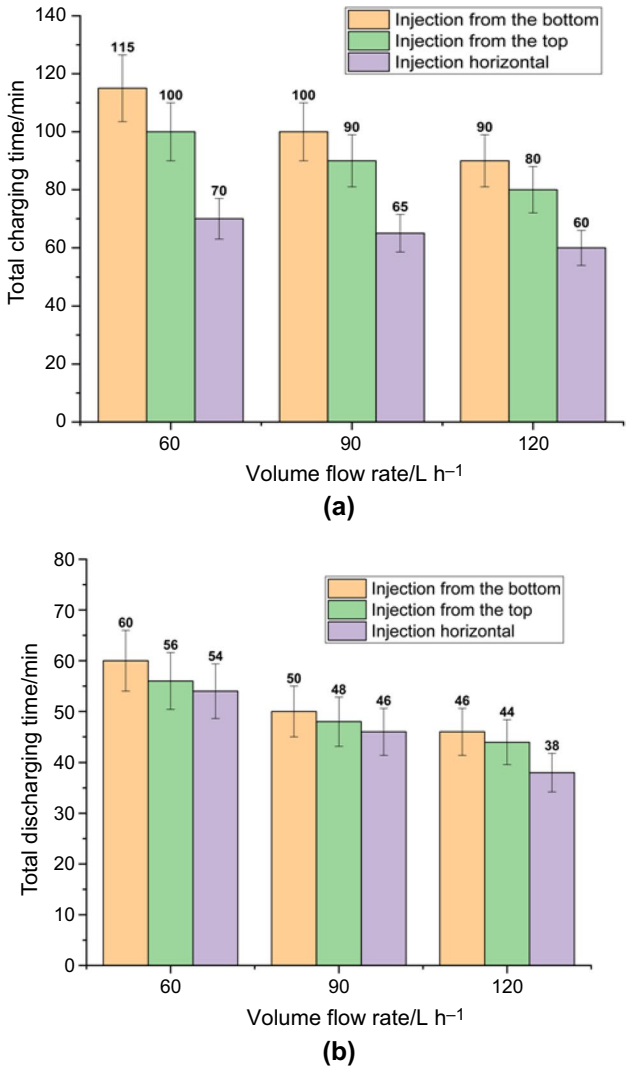


Fig. 13 Comparison of total time for three configurations, **a**) charging, **b**) discharging

K^{-1}at 120 L h^{-1}. In the top configuration, h remains at 0 W m^{-2} K^{-1} for all flow rates, as $T_{PCM,ave}$ does not exceed this range. The horizontal configuration starts at 490.58 W m^{-2} K^{-1} at 60 L h^{-1}, rising to 874.14 W m^{-2} K^{-1} at 90 L h^{-1} and 1092.31 W m^{-2} K^{-1} at 120 L h^{-1}.

Above 55 °C, the bottom configuration reaches 731.14 W m^{-2} K^{-1} at 60 L h^{-1} but drops to 0 W m^{-2} K^{-1} at 90 L h^{-1} due to $T_{PCM,ave}$ remaining below 55 °C, before increasing to 1806.34 W m^{-2} K^{-1}at 120 L h^{-1}. The top configuration remains at 0 W m^{-2} K^{-1}, while the horizontal setup records 649.23 W m^{-2} K^{-1} at 60 L h^{-1} before dropping to zero at 90 L h^{-1} and 120 L h^{-1}, indicating a lower average PCM temperature.

Overall, the findings confirm that increasing the flow rate enhances heat transfer performance across all configurations. Notably, the average heat transfer coefficient nearly doubles when the flow rate increases from 60 to 120 L h^{-1}, underscoring the significant impact of flow rate on heat transfer efficiency.

Figure 13a and b provide a summary of the total charge and discharge durations of the LHTES system under varying HTF flow rates and an inlet temperature of 70 °C. The experiments were conducted with a consistent initial RT50 temperature, examining an HTF inlet temperature of 70 °C and three volumetric flow rates: 60 L h^{-1}, 90 L h^{-1}, and 120 L h^{-1}. Analyzing these figures highlights three key observations:

Charging time decreases with increasing flow rate. In the bottom water injection configuration, recharge times are reduced from 115 min at 60 L h^{-1} to 90 min at 120 L h^{-1}. The top injection configuration requires 100 min

Table 3 Summary of experimental observations for charging and discharging

Charging process				
Injection		60 L h^{-1}	90 L h^{-1}	120 L h^{-1}
Horizontal	Time	70 min	65 min	60 min
	Evolution of melting front	Progression of injection towards output Upper part melted before lower part		
	Temperature distribution depending on position	Significant angular		
	Thermal stratification	Lightweight, warmer on the injection side		
Bottom	Time	115 min	100 min	90 min
	Evolution of melting front	From top to bottom		
	Temperature distribution depending on position	Axial quite marked from top to bottom		
	Thermal stratification	Restoration of thermal stratification through natural convection during phase change		
Top	Time	100 min	90 min	80 min
	Evolution of melting front	From top to bottom		
	Temperature distribution depending on position	Axial quite marked from top to bottom		
	Thermal stratification	Kept throughout the test		
Discharging process				
Injection		60 L h^{-1}	90 L h^{-1}	120 L h^{-1}
Horizontal	Time	54 min	46 min	38 min
	Evolution of melting front	/		
	Temperature distribution depending on position	/		
Bottom	Time	60 min	50 min	46 min
	Evolution of melting front	-Influence of the free surface from bottom to top and top to bottom		
	Temperature distribution depending on position	-Axial influence is very minimal -Impact of liquid level drop due to volume restriction		
Top	Time	56 min	48 min	44 min
	Evolution of melting front	-A radial solidification front is present over the entire length at the start of the test -The solidification then evolves from top to bottom		
	Temperature distribution depending on position	-Axial effects are minimal, except for the thermocouples positioned very close to the injection point -Natural convection influences the process at the start of the test		

at 60 L h^{-1} and 80 min at 120 L h^{-1}, while the horizontal configuration completes recharging in 70 min at 60 L h^{-1} and 60 min at 120 L h^{-1}. Similarly, discharge time also decreases as flow rate increases. In the bottom configuration, discharge times drop from 60 min at 60 L h^{-1} to 46 min at 120 L h^{-1}. The top configuration sees a reduction from 56 min at 60 L h^{-1} to 44 min at 120 L h^{-1}, while the horizontal setup improves from 54 min at 60 L h^{-1} to 38 min at 120 L h^{-1}.

The bottom water injection configuration results in longer charging times compared to the top and horizontal configurations. At a flow rate of 60 L h^{-1}, recharge times are 115 min for bottom injection, 100 min for top injection, and 70 min for horizontal injection, with similar trends observed across all flow rates. A similar pattern is evident in discharge times at 60 L h^{-1}, with durations of 60 min for bottom injection, 56 min for top injection, and 54 min for horizontal injection. These findings consistently highlight the impact of injection configuration on charge and discharge durations.

Higher HTF inlet temperatures lead to shorter charging times in the LHTES system by enhancing convective heat transfer. Elevated inlet temperatures significantly improve heat transfer rates, with the effect being particularly pronounced at lower HTF flow rates.

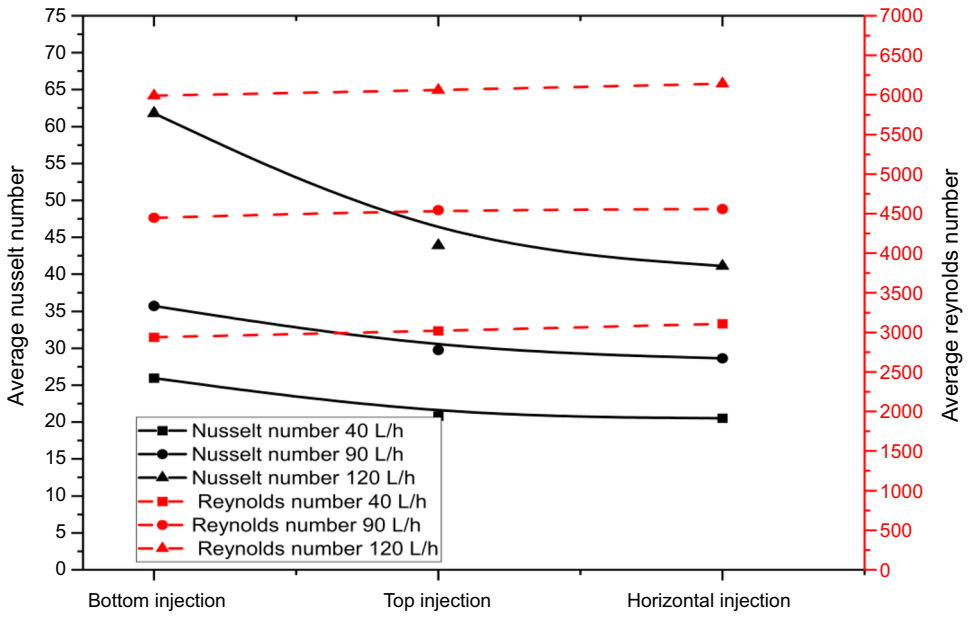


Fig. 14 Nusselt and Reynolds numbers for different injection configurations

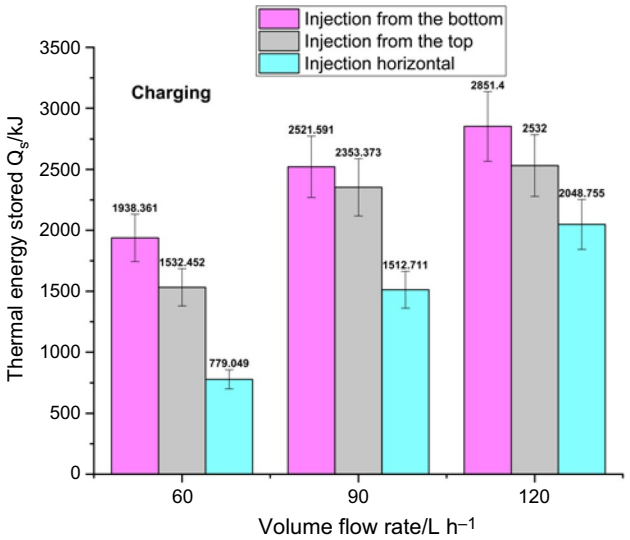


Fig. 15 Comparison of flow rates, corresponding average thermal energy stored for the considered water injection configurations

The experimental results in Table 3 highlight the significant influence of liquid movement within the PCM on heat transfer, with volume expansion playing a crucial role alongside natural convection. For industrial applications, top loading is the preferred method due to its shorter test durations and enhanced heat transfer efficiency. In contrast, horizontal and bottom loading can disrupt thermal stratification, impeding the formation of a thermal piston-type melting front, which is essential for accurately monitoring the charge state of the storage tank. Moreover, volume expansion in bottom or horizontal loading configurations increases the risk of damage to heat exchangers if a solid plug forms above the liquid PCM. Consequently, top loading emerges as the most effective approach, aligning with the findings of Longeon et al. [27] and Shokouhmand et al. [43].

The Reynolds number (Re) plays an important role in determining the flow behavior inside a heat exchanger. It helps identify whether the flow is laminar or turbulent, which directly influences heat transfer efficiency. Turbulent flow, associated with higher Reynolds numbers, generally promotes better mixing and enhances heat transfer. The Nusselt number (Nu) is equally important as it quantifies how much heat is transferred by convection compared to conduction. A higher Nusselt number indicates more efficient heat transfer, as it reflects the role of fluid movement in boosting convective heat transfer.

Analyzing Fig. 14 reveals key insights into the behavior of Re and Nu across different water injection configurations (bottom, top, and horizontal) and flow rates (60 L h^{-1}, 90 L h^{-1}, and 120 L h^{-1}). The Reynolds number increases with higher flow rates across all configurations, as illustrated in Fig. 14. In the bottom injection configuration, it rises from 2940 at 60 L h^{-1} to 5990 at 120 L h^{-1}, while the top injection sees an increase from 3021 to 6059, and the horizontal injection grows from 3111 to 6140. Similarly, Fig. 13 shows that the Nusselt number also rises with flow rate. For the bottom injection, it goes from 25.959 at 60 L h^{-1} to 61.81 at 120 L h^{-1}; for top injection, it increases from 20.816 to 43.914; and for horizontal injection, it rises from 20.513 to 41.105. These trends reveal an interesting relationship between the Reynolds and Nusselt numbers. Although the horizontal configuration demonstrates the highest Reynolds numbers, indicating more turbulent flow, it has the lowest Nusselt numbers, suggesting less efficient heat transfer. In contrast, the bottom injection configuration, with the lowest Reynolds

numbers, achieves the highest Nusselt numbers, indicating optimal heat transfer efficiency. Specifically, at 60 L h^{-1}, the average Reynolds numbers are 2940 for bottom, 3021 for top, and 3111 for horizontal injection, while the corresponding average Nusselt numbers are 25.959, 20.816, and 20.513, respectively. At 120 L h^{-1}, the Reynolds numbers rise to 5990, 6059, and 6140, while the Nusselt numbers are 61.81, 43.914, and 41.105.

This comparison highlights that increased turbulence in the horizontal configuration does not equate to improved heat transfer efficiency. The bottom injection configuration proves to be more effective in optimizing heat transfer, despite having lower turbulence. This underscores the need to consider both fluid dynamics and thermal efficiency when designing heat exchanger systems. This analysis offers a clearer and more physically grounded interpretation of the results. An increase in Reynolds number across all setups points to higher fluid velocities, typically associated with intensified turbulence. Yet, it is the bottom injection configuration that achieves the highest Nusselt number, even though its Reynolds number is comparatively lower. This might seem counterintuitive at first, but it can be understood by considering the combined effects of forced and natural convection.

In this specific arrangement, buoyancy forces appear to work in tandem with the imposed flow, helping the PCM circulate more effectively along the melting front. This interaction helps reduce the thickness of the thermal boundary layer, leading to better heat transfer performance. On the other hand, the horizontal and top injection setups tend to interfere with buoyancy-induced circulation, making it harder for a stable thermal boundary layer to form, which in turn limits heat transfer efficiency.

Figure 15 illustrates the relationship between flow rates and the thermal energy stored in the PCM for water temperatures of 70 °C across three injection configurations: bottom, top, and horizontal. The thermal energy is accumulated both sensibly in the solid and liquid phases of the PCM, as well as latently during the phase change. Initially, the hot water transfers energy that is absorbed sensibly by the solid PCM. As melting begins, a significant portion of this energy is used for the solid-to-liquid phase transition, while the liquid PCM simultaneously absorbs additional thermal energy sensibly. Over time, the total thermal energy stored increases, especially at a HTF temperature of 70 °C. However, once all solid PCM has undergone melting, the rate of energy storage slows as the remaining transferred energy is absorbed by the liquid PCM. This stored energy can later be retrieved when the solidification (discharging) mode is activated.

Notably, the thermal energy stored rises with higher flow rates. For instance, in the bottom injection configuration, at 60 L h^{-1}, the required recharge energy is 1938.361 kJ, which increases to 2851.4 kJ at 120 L h^{-1}. In the top configuration, the recharge energy drops from 1532.452 kJ at 60 L h^{-1} to 2532 kJ at 120 L h^{-1}. The horizontal setup shows a significant variation, with recharge energy increasing from 779.049 kJ at 60 L h^{-1} to 12,048.755 kJ at 120 L h^{-1}. Additionally, the bottom injection configuration consistently demonstrates higher thermal energy storage compared to both the top and horizontal configurations. At a $\dot{m} = 60$ L h^{-1}, the thermal energies stored are 1938.361 kJ for bottom, 1532.452 kJ for top, and 779.049 kJ for horizontal. At 120 L h^{-1}, the values are 2851.4 kJ for bottom, 2532 kJ for top, and 2048.755 kJ for horizontal.

Conclusions

In this study, a detailed model of a latent heat storage system was developed, featuring both horizontal and vertical tube heat exchangers, utilizing RT50 as the phase change material (PCM). The impact of two different HTF injection orientations on the melting duration of the PCM was systematically investigated, while varying the HTF flow rate and initial temperature conditions. Additionally, a comprehensive analysis was conducted to examine how the configuration of the heat exchangers, whether horizontal or vertical, affected the optimization of PCM charging and discharging times under both bottom and top injection scenarios. The experimental findings revealed several important insights:

- Increased HTF temperatures significantly enhanced the melting rate of the PCM. Specifically, raising the HTF temperature from 70 to 80 °C reduced the melting time by approximately 25%, from about 3600 s to 2700 s.
- A top HTF inlet promoted higher average PCM temperatures and shorter charging durations compared to a bottom inlet configuration.
- In the top injection setup, a flow rate of 120 L h^{-1} elevated the average PCM temperature to 58.92 °C with a charging time of just 90 min, compared to 50 °C and 80 min in the bottom configuration. Thus, employing a top injection configuration combined with a high HTF flow rate was recommended for optimizing the melting process.
- While bottom charging required a total time of 6000 s, top charging was faster, completing in 4800 s. Across all configurations, higher HTF flow rates enhanced thermal discharge efficiency by reducing the time needed to extract heat from the PCM.
- Increasing the flow rate from 60 to 120 L h^{-1} nearly doubled the average heat transfer coefficient. Discharge times were notably improved: in the bottom configuration, discharge took 60 min at 60 L h^{-1} and reduced to 46 min at 120 L h^{-1}; for the top configuration, dis-

charge times decreased from 56 to 44 min, while the horizontal configuration saw a reduction from 54 to 38 min.

- The bottom injection configuration consistently resulted in longer charging and discharging times compared to top and horizontal injection setups. At a flow rate of 60 L h^{-1}, recharge times were 115 min for bottom injection, 100 min for top injection, and 70 min for horizontal injection. Discharge times were 60 min for bottom, 56 min for top, and 54 min for horizontal injection.
- The bottom injection configuration, characterized by the lowest Reynolds numbers, demonstrated the highest Nusselt numbers, indicating superior heat transfer efficiency. Despite exhibiting lower turbulence, this configuration proved to be more effective in optimizing heat transfer performance. At 60 L h^{-1}, the bottom configuration had a Reynolds number of 2940 and a Nusselt number of 25.96, while the horizontal configuration, with the highest Reynolds number of 3111, had a lower Nusselt number of 20.51. At 120 L h^{-1}, the Reynolds numbers for all configurations increased, with the bottom injection still leading in Nusselt numbers (61.81), compared to 41.11 for the horizontal configuration.

This study offers valuable insights for optimizing latent heat storage systems, with practical implications across various industries. Horizontal configurations, with their fast charging and discharging capabilities, are particularly suited for systems requiring frequent cycling, such as solar energy storage and industrial waste heat recovery. Bottom injection setups, known for their high efficiency, are ideal for long-term heat storage, while top injection configurations enhance heat exchanger performance in HVAC systems. Additionally, the findings regarding the effects of flow rate and temperature provide useful guidance for designing more efficient PCM heat exchangers for industrial applications. Overall, this research significantly contributes to improving energy efficiency in renewable energy systems, building technologies, and industrial processes. Future research could explore the use of active heat transfer enhancements, such as fins or nanoparticles, to further boost performance. It would also be valuable to study long-term effects, including repeated thermal cycling, PCM aging, and potential leakage, to better understand system durability.

Funding Open access funding provided by the Scientific and Technological Research Council of Türkiye (TÜBİTAK).

Open Access This article is licensed under a Creative Commons Attribution 4.0 International License, which permits use, sharing, adaptation, distribution and reproduction in any medium or format, as long as you give appropriate credit to the original author(s) and the source, provide a link to the Creative Commons licence, and indicate if changes were made. The images or other third party material in this article are included in the article's Creative Commons licence, unless indicated otherwise in a credit line to the material. If material is not included in the article's Creative Commons licence and your intended use is not permitted by statutory regulation or exceeds the permitted use, you will need to obtain permission directly from the copyright holder. To view a copy of this licence, visit http://creativecommons.org/licenses/by/4.0/.

References

1. Fredi G, Dorigato A, Fambri L, Pegoretti A. Evaluating the multifunctional performance of structural composites for thermal energy storage. Polymers. 2021;13:3108.
2. Malik FK, Khan MM, Ahmed HF, Irfan M, Ahad IU. Performance characteristics of PCM based thermal energy storage system for fluctuating waste heat sources. Case Stud Therm Eng. 2022;34:102012.
3. Cao Z, Zhang G, Wu Y, Yang J, Sui Y, Zhao X. Energy storage potential analysis of phase change material (PCM) energy storage units based on tunnel lining ground heat exchangers. Appl Therm Eng. 2023;235:121403.
4. Mozafari M, Lee A, Cheng S. A novel dual-PCM configuration to improve simultaneous energy storage and recovery in triplex-tube heat exchanger. Int J Heat Mass Transfer. 2022;186:122420.
5. Chowdhury JI, Hu Y, Haltas I, Balta-Ozkan N, Varga L. Reducing industrial energy demand in the UK: a review of energy efficiency technologies and energy saving potential in selected sectors. Renew Sustain Energy Rev. 2018;94:1153–78.
6. Zhang S, Yan Y, Cheng Z, Wang F. Charging and discharging in thermal energy storage unit with fin-stone hybrid structure for enhancing heat transfer of phase change materials. Int J Heat Mass Transfer. 2024;224:125325.
7. Dong Y, Wang F, Yang L, et al. Thermal performance analysis of PCM capsules packed-bed system with biomimetic leaf hierarchical porous structure. J Therm Sci. 2021;30:1559–71.
8. Chen X, Li C, Yang Z, Dong Y, Wang F, Cheng Z, et al. Golf-ball-inspired phase change material capsule: experimental and numerical simulation analysis of flow characteristics and thermal performance. Energy. 2024;293:130595.
9. Alam MT, Raj A, Singh LK, Gupta AK. Configurational assessment of solidification performance in a triplex-tube heat exchanger filled with composite phase change material. Appl Therm Eng. 2023;230:120814.
10. Ajarostaghi SSM, Amirsoleymani A, Arıcı M, Dolati A, Amiri L. Thermal energy storage with PCMs: a comprehensive study of horizontal shell and multi-tube systems with finned design. J Energy Storage. 2023;72:108762.
11. Herbinger F, Groulx D. Experimental comparative analysis of finned-tube PCM-heat exchangers' performance. Appl Therm Eng. 2022;211:118532.
12. Zhang XY, Ge YT, Lang PY. Experimental investigation and CFD modelling analysis of finned-tube PCM heat exchanger for space heating. Appl Therm Eng. 2024;244:122731.
13. Talebizadehsardari P, Mahdi JM, Mohammed HI, Moghimi MA, Eisapour AH, Ghalambaz M. Consecutive charging and discharging of a PCM-based plate heat exchanger with zigzag configuration. Appl Therm Eng. 2021;193:116970.
14. Mahdi MS, Mahood HB, Khadom AA, Campbell AN, Hasan M, Sharif AO. Experimental investigation of the thermal performance of a helical coil latent heat thermal energy storage for solar energy applications. Therm Sci Eng Prog. 2019;10(2019):287–98.

15. Momeni M, Fartaj A. Numerical thermal performance analysis of a PCM-to-air and liquid heat exchanger implementing latent heat thermal energy storage. J Energy Storage. 2023;58:106363.
16. Bianco N, Fragnito A, Iasiello M, Mauro GM, Mongibello L. Multi-objective optimization of a phase change material-based shell-and-tube heat exchanger for cold thermal energy storage: experiments and numerical modeling. Appl Therm Eng. 2022;215:119047.
17. Ghasemi SE, Ranjbar AA. A novel numerical study on the melting process of phase change materials in a heat exchanger for energy storage. Numer Heat Transf, Part A: Appl. 2024;85(2):237–49.
18. Chandran KN, Jeong YS, Kim HG, Min JK, Ha MY. Investigation of the thermal exchange mechanism of PCM melting process in an LHTES with elliptic tube configurations inside a cylindrical shell. J Energy Storage. 2024;76:109838.
19. Hasan A. Thermal energy storage system with stearic acid as phase change material. Energy Convers Manag. 1994;35(10):843–56.
20. Hasan A. Phase change material energy storage system employing palmitic acid. Sol Energy. 1994;52(2):143–54.
21. Seddegh S, Wang X, Henderson AD. A comparative study of thermal behaviour of a horizontal and vertical shell-and-tube energy storage using phase change materials. Appl Therm Eng. 2016;93:348–58.
22. Cheng PS, Wong SC, Wu SK. Heat transfer phenomena and performance investigations for 3D fin-and-tube pulsating heat pipe heat exchanger under vertical and horizontal orientations. Therm Sci Eng Prog. 2024;56:103077.
23. Trp A, Lenic K, Frankovic B. Analysis of the influence of operating conditions and geometric parameters on heat transfer in water-paraffin shell-and-tube latent thermal energy storage unit. Appl Therm Eng. 2006;26:1830–9.
24. Joybari MM, Seddegh S, Wang X, Haghighat F. Experimental investigation of multiple tube heat transfer enhancement in a vertical cylindrical latent heat thermal energy storage system. Renew Energy. 2019;140:234–44.
25. Yang X, Yu J, Xiao T, Hu Z, He Y-L. Design and operating evaluation of a finned shell-and-tube thermal energy storage unit filled with metal foam. Appl Energy. 2020;261:114385.
26. Kurnia JC, Sasmito AP. Numerical investigation of heat transfer performance of a rotating latent heat thermal energy storage. Appl Energy. 2018;227:542–54.
27. Longeon M, Soupart A, Fourmigué J-F, Bruch A, Marty P. Experimental and numerical study of annular PCM storage in the presence of natural convection. Appl Energy. 2013;112:175–84.
28. Han G-S, Ding H-S, Huang Y, Tong L-G, Ding Y-L. A comparative study on the performances of different shell-and-tube type latent heat thermal energy storage units including the effects of natural convection. Int Commun Heat Mass Transf. 2017;88:228–35.
29. Moghaddam MAE, Ganji DD. A comprehensive evaluation of the vertical triplex-tube heat exchanger with PCM, concentrating on flow direction, nanoparticles and multiple PCM implementation. Therm Sci Eng Prog. 2021;26:101124.
30. Guo Z, Zhou W, Liu S, Kang Z, Tan R. Effects of geometric parameters and heat-transfer fluid injection direction on enhanced phase-change energy storage in vertical shell-and-tube system. Sustainability. 2023;15(17):13062.
31. Nie C, Liu J, Deng S. Effect of geometric parameter and nanoparticles on PCM melting in a vertical shell-tube system. Appl Therm Eng. 2021;184:116290.
32. Laouer A, Belhadj M, Rocha TTM, Teggar M, Arıcı M. Effect of partial cooling-heating configurations on the enhanced latent thermal energy storage performance. Appl Therm Eng. 2024;242:122438.
33. Lee YT, Liao YR, Chien LH, Cheung FB, Yang AS. Performance enhancement of latent heat thermal energy storage systems via dynamic melting process of PCM under different control strategies. Appl Therm Eng. 2025;259:124903.
34. Ali SA, Habib K, Younas M, Rahman S, Das L, Rubbi F, et al. Advancements in thermal energy storage: a review of material innovations and strategic approaches for phase change materials. Energy Fuels. 2024;38(20):19336–92.
35. Chen J, Kou Y, Zhang S, Zhang X, Liu H, Yan H, et al. Spatiotemporal utilization of latent heat in erythritol-based phase change materials as solar thermal fuels. Angew Chem Int Ed Engl. 2024;63(16):e202400759.
36. Dheyab HS, Al-Jethelah M, Ibrahim TK, Chtourou S, Baccar M. Closed solar air heater system integrated with PCM (RT42 and RT50) in a thermal storage-finned heat exchanger unit. Tikrit J Eng Sci. 2023;30(3):27–37.
37. Lu B, Zhang Y, Sun D, Yuan Z, Yang S. Experimental investigation on thermal behavior of paraffin in a vertical shell and spiral fin tube latent heat thermal energy storage unit. Appl Therm Eng. 2021;187:116575.
38. Hosseini MJ, Rahimi M, Bahrampoury R. Experimental and computational evolution of a shell and tube heat exchanger as a PCM thermal storage system. Int Commun Heat Mass Transfer. 2014;50:128–36.
39. Martinelli M, Bentivoglio F, Caron-Soupart A, Couturier R, Fourmigue JF, Marty P. Experimental study of a phase change thermal energy storage with copper foam. Appl Therm Eng. 2016;101:247–61.
40. Hassan AK, Abdulateef J, Mahdi MS, Hasan AF. Experimental evaluation of thermal performance of two different finned latent heat storage systems. Case Stud Therm Eng. 2020;21:100675.
41. Mahdi MS, Mahood HB, Campbell AN, Khadom AA. Experimental study on the melting behavior of a phase change material in a conical coil latent heat thermal energy storage unit. Appl Therm Eng. 2020;175:114684.
42. Kalapala L, Devanuri JK. Influence of operational and design parameters on the performance of a PCM based heat exchanger for thermal energy storage–a review. J Energy Storage. 2018;20:497–519.
43. Shokouhmand H, Kamkari B. Numerical simulation of phase change thermal storage in finned double-pipe heat exchanger. Appl Mech Mater. 2012;232:742–6.

Publisher's Note Springer Nature remains neutral with regard to jurisdictional claims in published maps and institutional affiliations.